CeF_3-TbF_3-YF_3 nanoparticles for ratiometric temperature sensing

Pudovkin M.S*., Kalinichenko S.I., Nizamutdinov A.S.

Corresponding author:

*Pudovkin M.S. Email: jaz7778@list.ru

Kazan Federal University, 18 Kremlyovskaya str, Kazan, 420008, Russian Federation

Full postal address: 18th Kremlyovskaya street. Kazan 420008, Russian Federation, Institute of physics, Department of quantum electronics and radiospectroscopy (office 168)

Keywords

Luminescent thermometry, LIR, ratiometric temperature sensing, Ce^{3+}/Tb^{3+}.

Highlights

The $Ce_{0.5}Y_{0.5-X}Tb_XF_3$ nanoparticles demonstrated dependence of spectral shape on temperature (303 – 523 K range)

The temperature sensitivity of intensity ratio (LIR) is explained by phonon-assisted energy transfer ET (Ce^{3+}-Tb^{3+})

The LIR shape dependence on Tb^{3+} concentration is explained by competition between phonon-assisted ET (Ce^{3+}-Tb^{3+}) and cross-relaxation (Tb^{3+}-Tb^{3+})

Abstract

The $Ce_{0.5}Y_{0.5-X}Tb_XF_3$ (X = 0.01, 0.02, 0.05, 0.1, and 0.5) nanoparticles demonstrated a single-phase hexagonal structure corresponding to CeF_3 host. The average diameter was 15±1 nm. Under Ce^{3+} excitation at 266 nm, the luminescence peaks of (5d – 4f) Ce^{3+} and $^5D_4$ – ^4F_J (J = 6, 5, 4, and 3) Tb^{3+} were observed. The emission peaks from $^5D_3$ level of Tb^{3+} were not observed. We took the luminescence integrated intensity ratio (LIR) of Ce^{3+} and Tb^{3+} peaks as a temperature-dependent parameter (303 – 523 K range). The LIR functions decay with the temperature increase. Indeed, with the temperature rise, the depopulation rate of Ce^{3+} excited state by Tb^{3+} becomes higher (phonon-assisted process). Thus, the I_{Ce}/I_{Tb} decreases. However, the rate of the LIR decay decreases with the increase of Tb^{3+} concentration. It was suggested, that this phenomenon is related to the presence of two competing processes populating the $^5D_4$ state of Tb^{3+}. There are phonon-assisted non-radiate transition from $^5D_3$ to $^5D_4$ of Tb^{3+} and cross-relaxation between Tb^{3+} ions, which was considered less temperature-dependent. The contribution of less temperature-dependent cross-relaxation process to the population of $^5D_4$ increases with the Tb^{3+} concentration increase compared to $^5D_3$ – $^5D_4$ non-radiative transition. More significant contribution of the cross-relaxation leads to the decrease in the LIR descent rate. The maximum S_a and S_r values were 0.19 K^{-1} and 1.74 %/K at 303 K, respectively.

1. Introduction

Remote temperature sensing using luminescent inorganic nano- or microsized phosphors is considered an auspicious way to control the temperature of biological objects, the heating process during hyperthermia, and micro-circuit temperature mapping [1]–[5]. To perform precise and reliable measurements, the phosphors should have parameters of their luminescence that are highly dependent on temperature. Among these parameters, the shape of the luminescence spectrum seems to be very attractive. In this case, the temperature-dependent parameter is the integrated intensity ratio (LIR) between two luminescence peaks. Such parameter as LIR is independent of fluctuations in exciting irradiation power density compared to such parameter as luminescence intensity. To increase the LIR temperature sensitivity, the search for materials having at least two interdependent luminescence peaks is a highly challenging task. Compared with other luminescent materials (e.g., organic dye, quantum dots, etc.), rare-earth-doped luminescent materials have many advantages, such as sharp emission and long luminescence lifetime, good photochemical and thermal stability, lack of photobleaching etc [6], [7]. In addition, REF_3 are considered low-toxic for eukaryotic cells [8], [9]. Such ions as Pr^{3+} [10], Dy^{3+} [11], [12], Nd^{3+} [13], [14], and Er^{3+} [15] demonstrate notable LIR sensitivities. This temperature sensitivity is explained by the presence of two electron levels that share their populations according to the Boltzmann law [16]. These phosphors are classified as single-doped. The LIR temperature sensitivity here depends on the energy gap between thermally coupled values. In particular, for Pr^{3+} ions ($\Delta E \sim 500$ cm^{-1}) the absolute temperature sensitivity is around 0.01 K^{-1} at 300 K. These values are quite competitive; however, it is difficult to manipulate the electron level structure of the rare-earth ions. For this reason, the probability of increasing of the single-doped phosphor temperature sensitivity by some external features (host, morphology of nanosized particles, etc.) is limited. In its turn, there is a huge class of promising materials called double-doped phosphors [1]. Here, one ion serves as a donor, and the second serves as an acceptor.

However, in these systems back energy transfer from donor to acceptor is also possible [17], [18].

The temperature sensitivity of their spectral-kinetic characteristics is based on several physical processes, including phonon-assisted energy transfer from donor to acceptor and vice versa, energy diffusion, phonon-assisted cross-relaxation, temperature expansion of the host, et al. The higher temperature sensitivity can be achieved by using a proper combination of the above-mentioned processes. The contribution of each process to temperature sensitivity can be manipulated by the concentrations of both donor and acceptor ions and the choice of the host. For instance, for the Nd^{3+}/Yb^{3+} ion pair under excitation of Nd^{3+} there are energy transfer from Nd^{3+} to Yb^{3+}, back energy transfer from Yb^{3+} to Nd^{3+}, and energy diffusion between Yb^{3+} ions [17]. The energy exchange processes between Nd^{3+} and Yb^{3+} ions are phonon-assisted, hence, the probability of these processes increases with the temperature increase. For these reasons, the intensity of Yb^{3+} rises with the temperature increase compared to Nd^{3+} one. Back energy transfer neutralizes the difference in behavior of Nd^{3+} and Yb^{3+} which leads to the reduction of temperature sensitivity. In turn, back energy transfer and energy diffusion are competitive processes. The increase of Yb^{3+} concentration leads to the increase of energy diffusion probability, which decreases the probability of back energy transfer. Thus, the temperature sensitivity can be maximized by the choice of ion concentrations. The same double-doped phosphors, such as Pr^{3+}/Yb^{3+} [19], Tb^{3+}/Eu^{3+} [20], and Tm^{3+}/Yb^{3+} [21] were studied earlier. The above-mentioned systems have such disadvantage as spectral overlap of heteronymous ion emissions (except for the Tm^{3+}/Yb^{3+} ion pair [21]). It leads to some difficulties in the definition of emission boundaries resulting in lower accuracy.

The systems based on the Ce^{3+}/Tb^{3+} ion pair demonstrate good signal differentiability, which is important for clear LIR definition. It is also considered a promising material for temperature sensing. The Nd^{3+}/Yb^{3+}, Pr^{3+}/Yb^{3+}, Tb^{3+}/Eu^{3+}, and Tm^{3+}/Yb^{3+} ions with $4f^n$ electronic configurations demonstrate a weak electron-phonon coupling, while Ce^{3+} ions with parity allowed transitions between

5d and 4f configurations have a strong electron-lattice interaction. Hence, the Ce^{3+} emission (5d/4f) could be easily affected by surrounding temperature, making this ion a very promising candidate for optical temperature sensing [22]–[24]. The ET from Ce^{3+} to Tb^{3+} is phonon-assisted, which also provides temperature-dependent spectral characteristics of Ce^{3+}/Tb^{3+} doped phosphors.

The objective of this work was to demonstrate the applicability of $Ce_{0.5}Y_{0.5-X}Tb_XF_3$ nanoparticles for ratiometric optical temperature sensing. The main novelty of the article is that we present a concentration series of the Ce^{3+}/Tb^{3+} system via varying Tb^{3+} concentration.

The tasks were:

Synthesis of $Ce_{0.5}Y_{0.5-X}Tb_XF_3$ (X = 0.01, 0.02, 0.05, 0.1, and 0.5) nanoparticles (5 samples).

Physical-chemical characterization was carried out using transmission electron microscopy, X-ray diffraction, and laser absorption spectroscopy.

Spectral characterization of the samples in the 303 – 520 K temperature range.

2. Materials and methods

The $Ce_{0.5}Y_{0.5-X}Tb_XF_3$ (X = 0.01, 0.02, 0.05, 0.1, and 0.5) nanoparticles were synthesized via the co-precipitation method with subsequent microwave treatment. The detailed synthesis procedure is described in our previous work [25] as well as in the materials and methods part of the supplementary file. The luminescence excitation was carried out via 266 nm laser, the 4th harmonic of YAG:Nd laser from Lotis TII LS-2147, (pulse duration and repetition were 10 ns and 10 Hz, respectively). The spectra were detected using StellarNet CCD spectrometer. The luminescence decay curves we registered via monochromator connected with photomultiplier tube FEU-100 and digital oscilloscope Rhode&Schwartz with 1 GHz bandwidth. Physical characterization of the sapples was performed with Bruker D8 diffractometer with Cu K_α-radiation and Hitachi HT7700 Exalens transmission electron microscope (TEM)) with accelerating voltage of 100 kV in

TEM mode. The sample preparation: the suspension (10 microliters) was placed on a formvar/carbon lacey 3 mm copper grid; drying was performed at room temperature. After drying, the grid was placed in a transmission electron microscope using a special holder for microanalysis. The analysis was held at an accelerating voltage of 100 kV in TEM mode. The average diameter of the nanoparticles was estimated from the TEM images using the ImageJ software. The statistics are based on the analysis of 160 nanoparticles. Histogram plots were obtained with the OriginPro software. To get the diameter (D) of the nanoparticles, the area (in squire nanometers) of each nanoparticle from TEM image was equated to the area of a circle $\pi \cdot D^2/4$, where $\pi = 3.14$, and D is the diameter. The obtained histogram was approximated via Lognornal function where ±1 standard deviation was determined.

3. Results and discussion

3.1 Physica-chemacl characterization of $Ce_{0.5}Y_{0.5-X}Tb_XF_3$ nanoparticles

The TEM image of $Ce_{0.5}Y_{0.5-X}Tb_XF_3$ (X = 0.01) nanoparticles and size distribution histogram are represented in Figure 1 **a** and **b**, respectively.

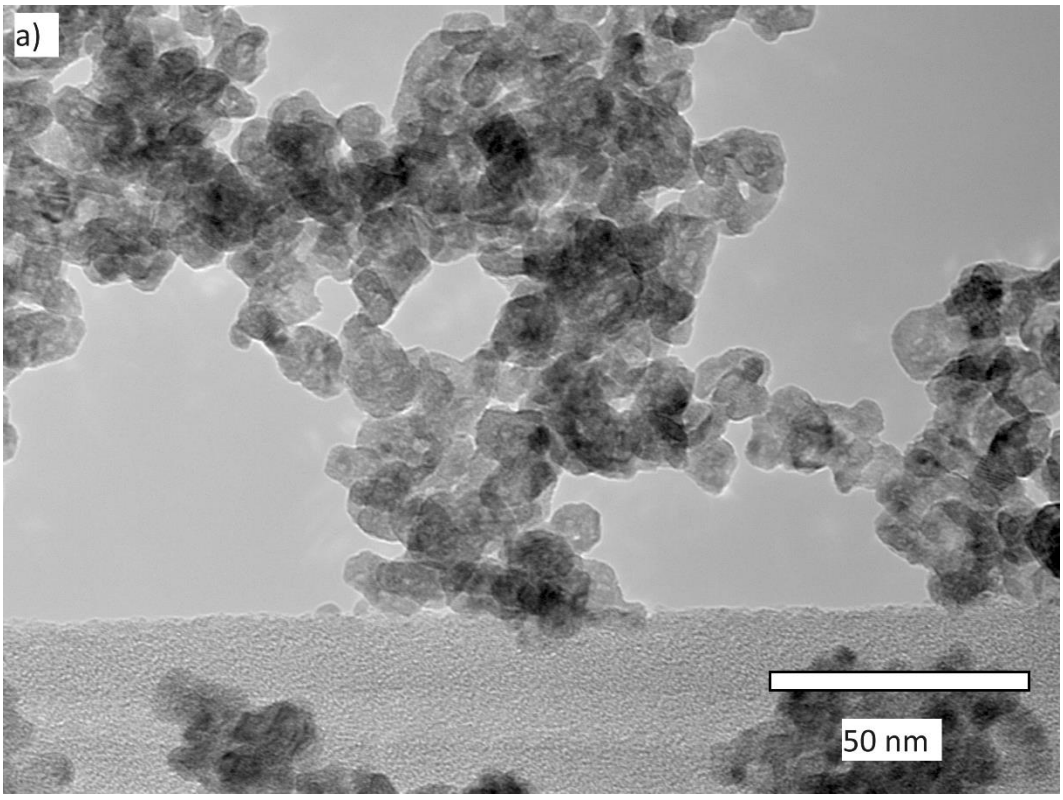

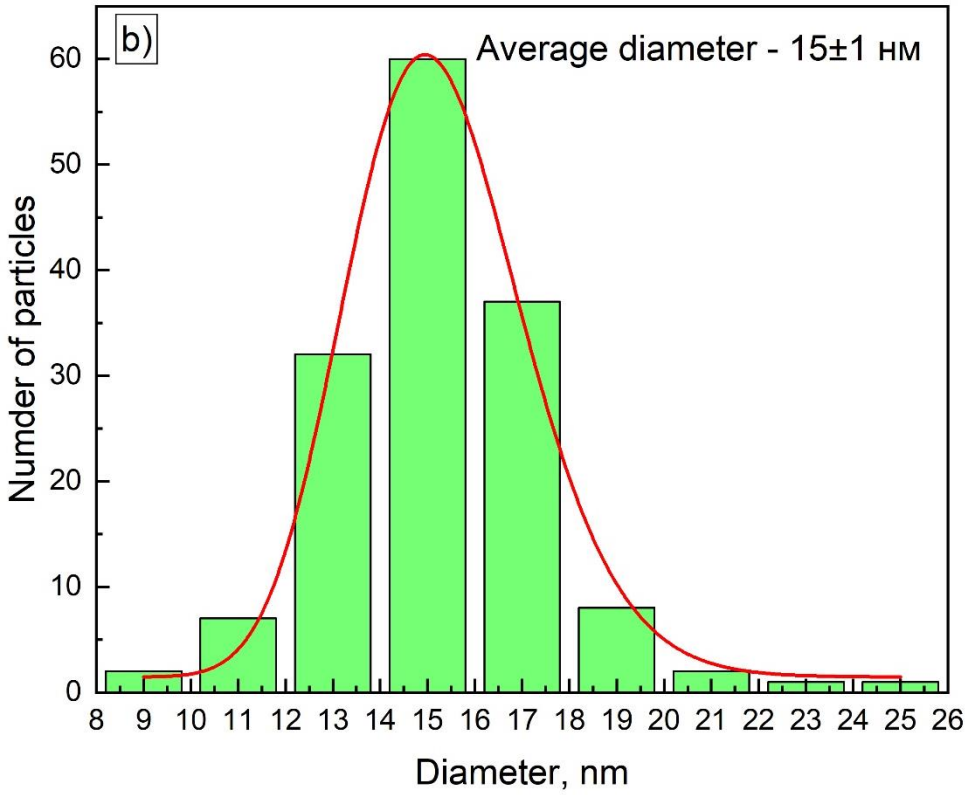

Figure 1. The TEM image of $Ce_{0.5}Y_{0.5-X}Tb_XF_3$ (X = 0.01) nanoparticles (a) and size distribution histogram (b)

It can be seen that the nanoparticle shape is not perfectly regular. The average diameter is 15±1 nm. The width at half maximum of the size distribution histogram is around 5 nm. Such nano-sized nanoparticles can be utilized in temperature mapping with submicron resolution. The phase composition of the nanoparticles was confirmed via the X-ray diffraction method (XRD). The representative XRD pattern of $Ce_{0.5}Y_{0.5-X}Tb_XF_3$ (X = 0.01) nanoparticles is shown in Figure 2.

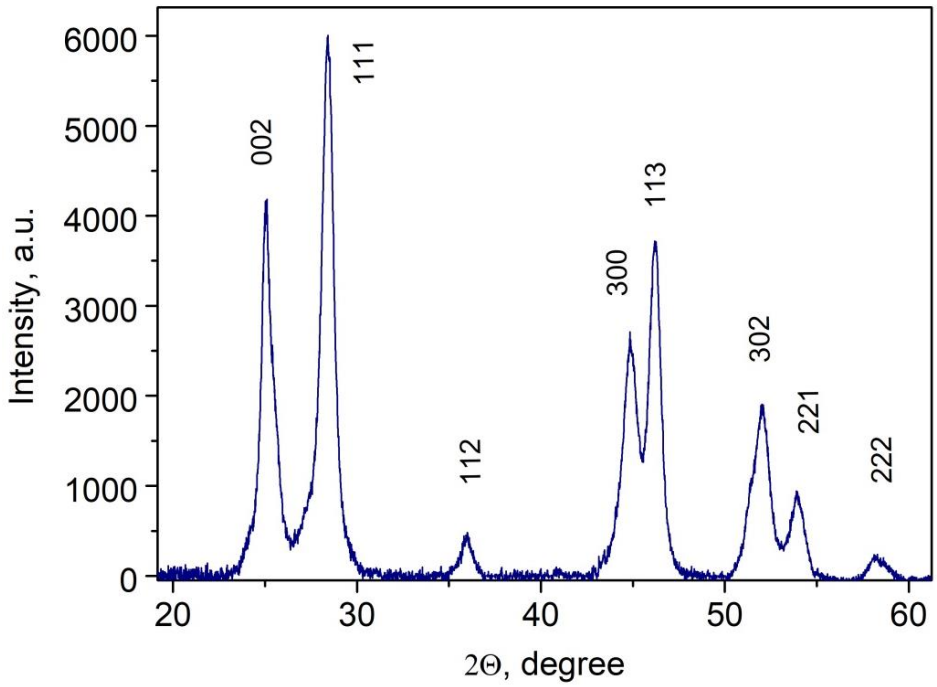

Figure 2. The XRD pattern of $Ce_{0.5}Y_{0.5-X}Tb_XF_3$ (X = 0.01) nanoparticles.

Despite the complex composition of the $Ce_{0.5}Y_{0.5-X}Tb_XF_3$ nanoparticles, they demonstrate a single-phase hexagonal structure corresponding to the CeF_3 host. Peaks from the impurity phases or amorphous phases were not observed. According to our previous work, even $Ce_{0.5}Y_{0.5-X}Tb_XF_3$ (X=0.15) nanoparticles had the same hexagonal structure [26].

The energy level diagram of Ce^{3+}/Tb^{3+} system and room temperature luminescence spectra normalized at Ce^{3+} peak are represented in Figure 3.

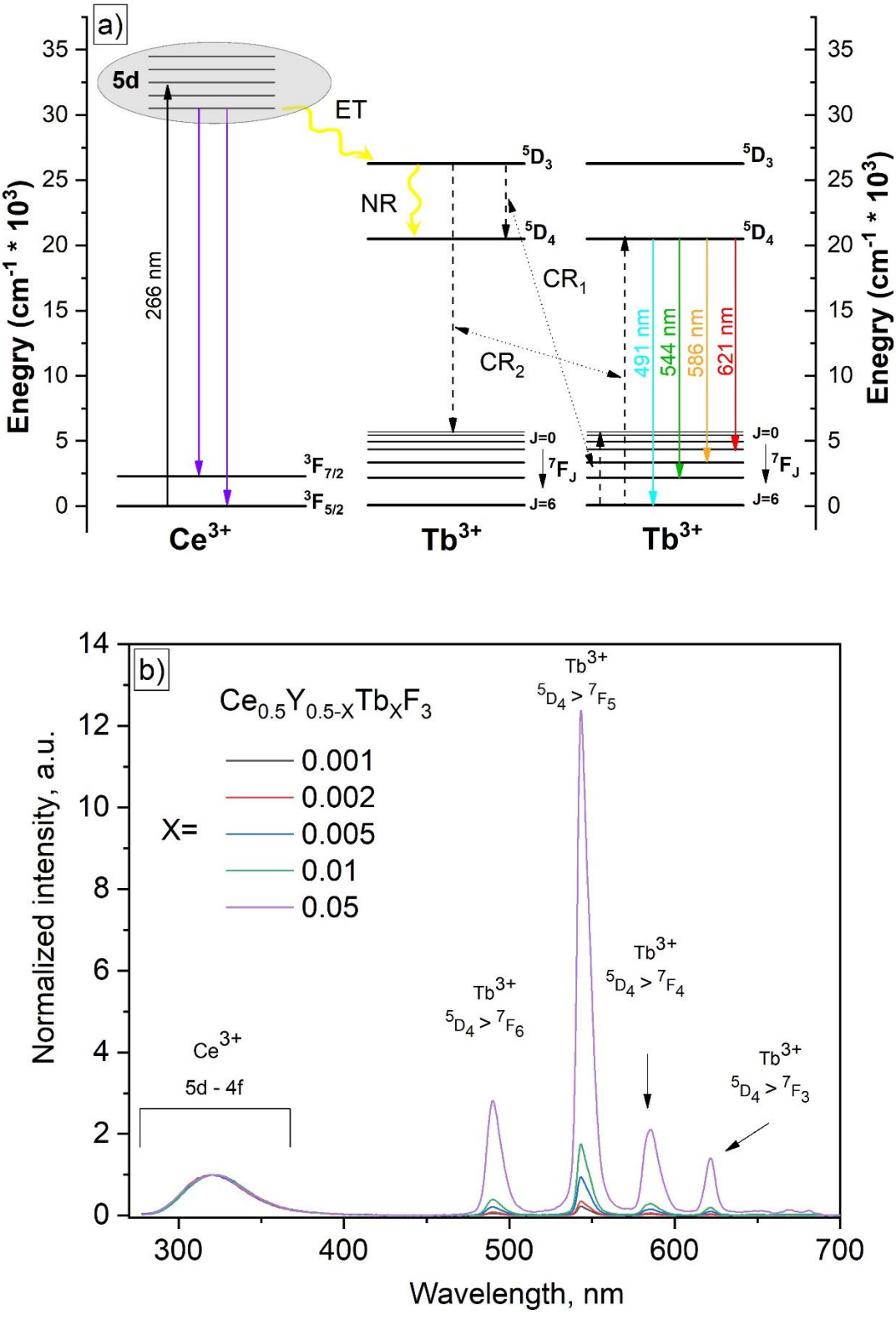

Figure 3. Energy level diagram of Ce^{3+}/Tb^{3+} system (a) and room temperature luminescence spectra of $Ce_{0.5}Y_{0.5-X}Tb_XF_3$ nanoparticles normalized at Ce^{3+} peak (b). Excitation wavelength 266 nm corresponds to 4f – 5d absorption band of Ce^{3+}

The optical excitation is performed at 266 nm (4f – 5d absorption band of Ce^{3+}). All the luminescence peaks are interpreted as radiative transitions from 5d of Ce^{3+} and $^5D_4$ – ^4F_J (J=6, 5, 4, and 3) of Tb^{3+}. The emission peaks from the $^5D_3$-excited state of Tb^{3+} were not observed. Probably, there are non-radiative transitions (denoted as NR in Figure 3a) from $^5D_3$ to $^5D_4$. It is seen that the intensity of Tb^{3+} emission rises compared to the Ce^{3+} one with the increase of Tb^{3+} concentration. It indicates the more efficient excitation energy transfer (denoted as ET in Figure 3a) from Ce^{3+} to Tb^{3+} with the increase of Tb^{3+} concentration. In addition, there is no spectral overlap between Ce^{3+} and Tb^{3+} emissions, which is important for precise temperature sensing. The cross-relaxation processes are discussed below (after Figure 5).

3.2 Temperature-dependent spectral characterization of $Ce_{0.5}Y_{0.5-X}Tb_XF_3$ nanoparticles

The integrated intensity dependencies (not normalized) on temperature for $Ce_{0.5}Y_{0.5-X}Tb_XF_3$ nanoparticles are presented in Figure 4a. The normalized at 544 nm peak (Tb^{3+}) luminescence spectra of $Ce_{0.5}Y_{0.5-X}Tb_XF_3$ (X = 0.01) nanoparticles detected in the 303 – 523 K temperature range are represented in Figure 4b. The rest of the intensity dependencies and spectra are represented in Figures S1a and S1b of the supplementary file, respectively.

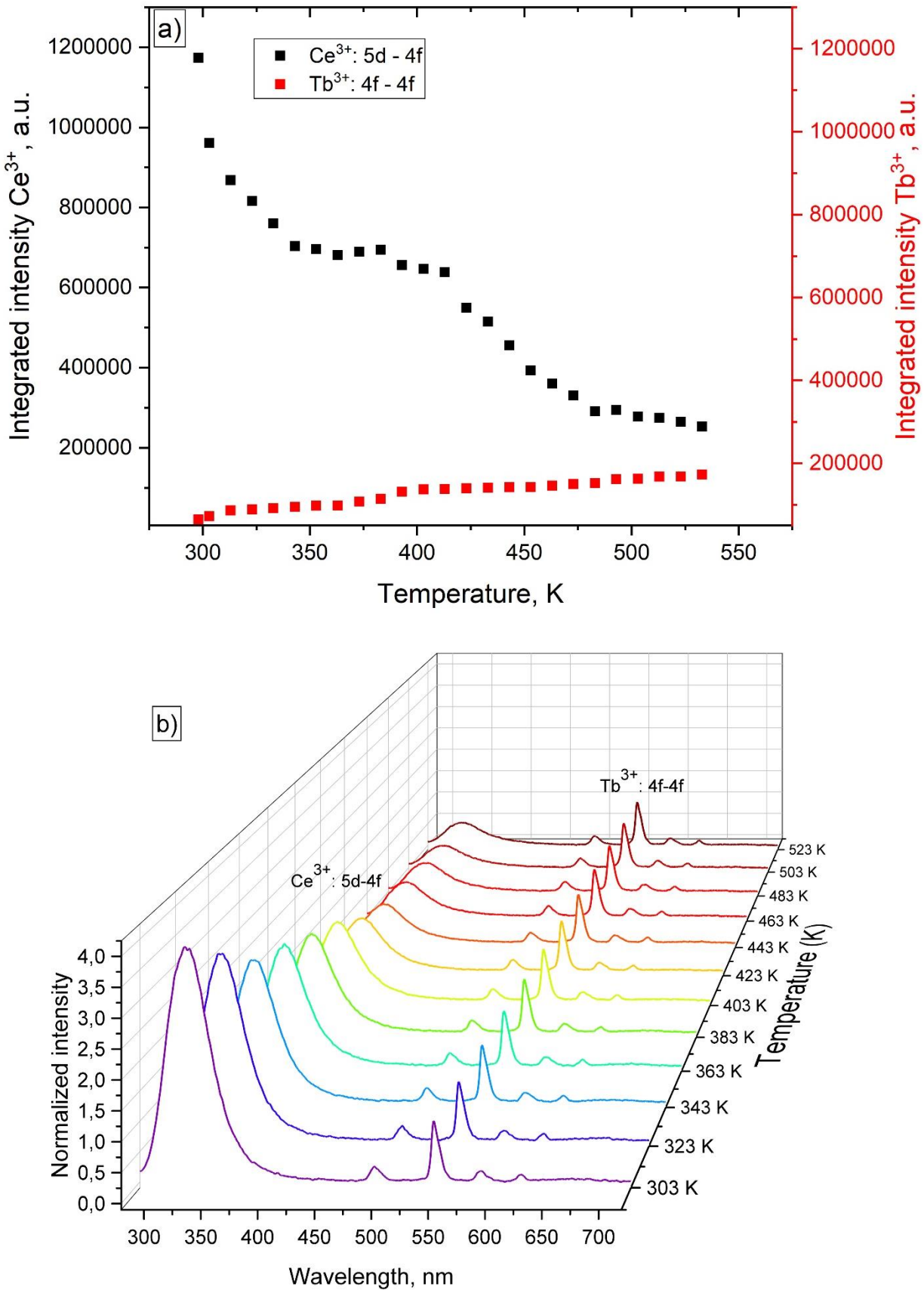

Figure 4. The integrated intensity dependences (not normalized) on temperature (a) and the normalized spectra at 544 nm peak (Tb^{3+}) luminescence

spectra of $Ce_{0.5}Y_{0.5-X}Tb_XF_3$ (X = 0.001) nanoparticles (b) detected in the 303 – 523 K temperature range. Excitation wavelength 266 nm corresponds to 4f – 5d absorption band of Ce^{3+}

It can be seen, that the intensity of Ce^{3+} emission decreases with the temperature increase compared to Tb^{3+} one. In its turn, the Tb^{3+} luminescence intensity rises with the temperature increase for the samples having X = 0.001, 0.002, and 0.005 amounts of Tb^{3+}. The $Ce_{0.5}Y_{0.5-X}Tb_XF_3$ (X = 0.01 and 0.05) nanoparticles demonstrate an opposite tendency. In particular, both Ce^{3+} and Tb^{3+} intensities decrease with the temperature increase. One of the possible mechanisms explaining the observed phenomenon is the phonon-assisted character of energy transfer from Ce^{3+} to Tb^{3+}. The probability of phonon appearance increases with the temperature increase, which leads to a more efficient depopulation of Ce^{3+} excited state by Tb^{3+}. However, at higher Tb^{3+} concentrations, the energy migration between Tb^{3+} ions appears. In this case, the excited state of Tb^{3+} can undergo radiative transitions or can be quenched by defects. This quenching by defects is phonon-assisted and temperature-dependent. It seems, that the samples demonstrating opposite behavior of both Ce^{3+} and Tb^{3+} intensities are capable of demonstrating higher temperature sensitivities. It should be noted, that the Tb^{3+} spectral shape is independent of temperature. It can be attributed to the absence of thermally coupled electron levels. To provide a deeper discussion of the temperature dependence of the spectra as well as estimate the nano-thermometer's performance we took the luminescence integrated intensity ratio (LIR) of Ce^{3+} and Tb^{3+} luminescence peaks as a temperature-dependent parameter. Since the Tb^{3+} luminescence (four peaks) is attributed to the radiative transitions from one excited energy level ($^5D_4$) to four lower energy ones, we used a sum of intensities of the four Tb^{3+} peaks ($^5D_4$ – ^4F_J (J=6, 5, 4, and 3)). As it was mentioned above, the temperature dependence of the spectral shape can be explained by the presence of at least two phonon-assisted energy transfer processes. More specifically, phonon-assisted energy transfer from Ce^{3+} to Tb^{3+} and the non-radiative transitions from $^5D_3$ to $^5D_4$ of Tb^{3+}.

The LIR functions for all the samples are presented in Figure 5.

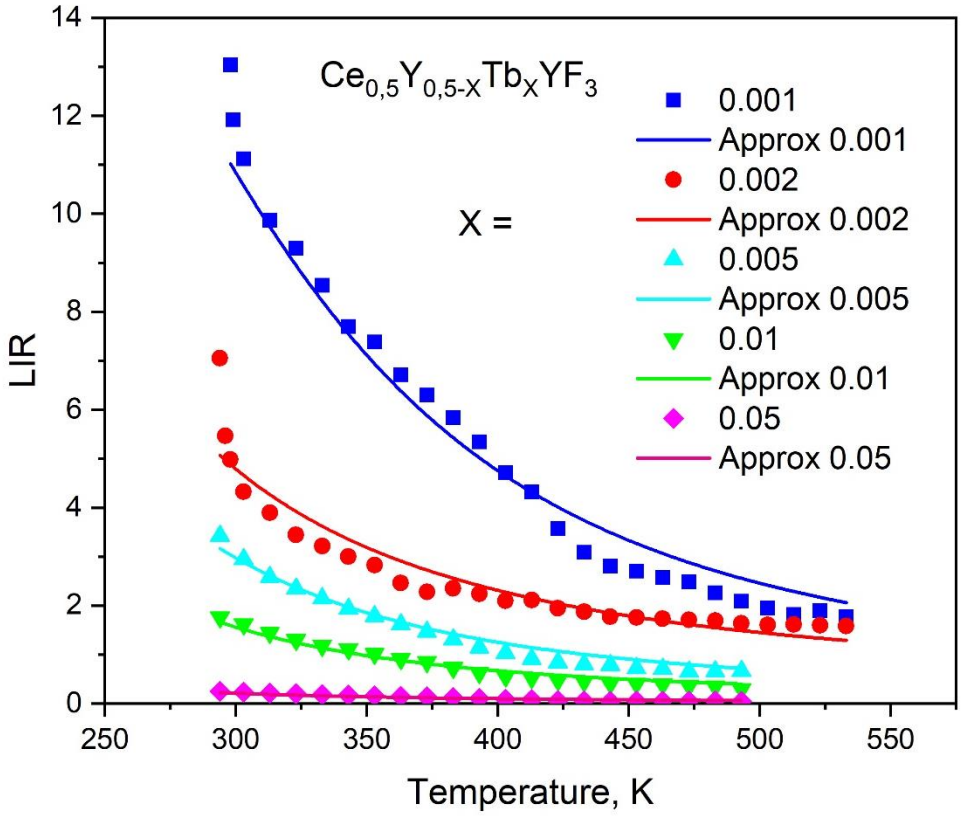

Figure 5. The approximated LIR (I_{Ce}/I_{Tb}) dependences of $Ce_{0.5}Y_{0.5-X}Tb_XF_3$ (X = 0.01, 0.02, 0.05, 0.1, and 0.5) nanoparticles

Predictably, the LIR functions decay with the temperature increase. Indeed, as the energy transfer efficiency increases the depopulation rate of Ce^{3+} by Tb^{3+} becomes higher. In its turn, the population of $^5D_4$ of Tb^{3+} becomes more effective. Thus, the I_{Ce}/I_{Tb} decreases. However, the shape of the LIR function strongly depends on Tb^{3+} concentration. Specifically, the rate of the LIR descent decreases with the increase of Tb^{3+} concentration. The observed tendencies are unlike the above-mentioned ion pairs (Nd^{3+}/Yb^{3+} [27] Pr^{3+}/Yb^{3+} [28], and Tm^{3+}/Yb^{3+} [21]) where LIR ($I_{donor}/I_{aceptor}$) also decays without such notable dependence on ion concentrations. According to the literature data, in the studied Ce^{3+}/Tb^{3+} system, the acceptor ion (Tb^{3+}) is capable of cross-relaxation [29] unlike such widespread acceptor as Yb^{3+}. In the literature, there are two proposed cross-relaxation schemes: $^5D_3 - {}^5D_4 + {}^7F_4 - {}^7F_0$ and $^5D_3 - {}^7F_0 + {}^7F_4 - {}^5D_4$ (Figure 3 a). Both mechanisms populate $^5D_4$ level. Moreover, in our previous work [26], we detected, that luminescence decay time of $^5D_4$ level of Tb^{3+} (λ_{em} = 541 nm, $^5D_4 - {}^7F_5$

transition) for $Ce_{0.5}Y_{0.5-X}Tb_XF_3$ nanoparticles rises with the Tb^{3+} concentrations increase for X = 0.005, 0.01, and 0.05), which can be related to the constant population of the $^5D_4$ level via cross-relaxation. It extends the decay time. In addition, we did not find that these cross-relaxation processes were phonon-assisted. Suggestively, the efficiency of cross-relaxation has a weak temperature dependence. Thus, there is a competition between cross-relaxations and $^5D_3$ – $^5D_4$ non-radiative transition in the population of the $^5D_4$ excited state. The cross-relaxation seems to be a low temperature-dependent process compared to phonon-assisted non-radiative transition. Hence, the contribution of the less temperature-dependent cross-relaxation process into the population of $^5D_4$ increases with the Tb^{3+} concentration increase compared to $^5D_3$ – $^5D_4$ non-radiative transition. This competition leads to the decrease in the rate of the LIR descent with the increase of Tb^{3+} concentration. Also, as it was mentioned above the Ce^{3+} intensity decreases with the decrease of temperature, in its turn, with the increase of temperature the Tb^{3+} intensity for X = 0.001, 0.002, and 0.005 rises. For X = 0.01 and 0.05 the opposite tendency is observed. It can be suggested, that for the higher Tb^{3+} concentrations, the concentration quenching occurs. This quenching happens due to excitation energy migration between Tb^{3+} ions with subsequent multiphonon quenching on defects [30]. This process is more efficient at higher temperatures and can contribute to the decrease of Tb^{3+} intensity (X = 0.01 and 0.05) with the increase of temperature. This process has a negative impact on the temperature sensitivity.

For calculating such important characteristics as absolute (S_a) and relative (S_r) temperature sensitivities, the approximation function should be determined. To approximate the LIR functions, we used a conventional dual-center emission Mott–Seitz model for competition between radiative and non-radiative transitions of doping ions. The LIR = I_1/I_2 (I_1 and I_2 are the luminescence intensities of two different doping ions, Ce^{3+} and Tb^{3+}, respectively) can be expressed using the equations [28], [1], [2]:

$$\Delta = \frac{\Delta_0}{1+\sum_i \alpha_i \exp(-\frac{\Delta E_i}{k_B T})} \quad (1)$$

Δ_0 is the thermometric parameter at T =0 K; $\alpha = W_0/W_R$ is the ratio between the non-radiative rates (W_0 at T = 0 K) and radiative rates (W_R), T is the absolute temperature (K), k_B is the Boltzmann constant, and ΔE is the activation energy of the non-radiative process, and index *i* is a number of the non-radiative processes. The scheme of the non-radiative process is presented in Figure 3a. To simplify the approximation function and calculate such important parameters as absolute and relative sensitivities, we took into consideration one effective non-radiative process describing phonon-assisted energy transfer from Ce^{3+} to Tb^{3+}:

$$\Delta = \frac{I_{Ce}}{I_{Tb}} = \frac{\Delta_0}{1 + \alpha \cdot exp\left(-\frac{\Delta E}{k_B T}\right)} \quad (2)$$

The fitting parameters are presented in Table S1. We try not to change Δ_0 and α significantly, at least keeping the order of magnitude. The values of the activation energy slightly decrease with the Tb^{3+} content increase. Probably, it can be related to the above-mentioned suggestion, that the contribution of non-phonon-assisted cross-relaxation processes rises and it is easier to depopulate higher excited states of Tb^{3+} without phonons. It can be seen, that the best approximation is achieved for $Ce_{0.5}Y_{0.5-X}Tb_XF_3$ (X = 0.05, 0.1, and 0.5). It is difficult to explain this observation; however, it can be suggested, that the chosen model (equation 2) describes double-doped systems where donors and acceptors interact with each other [1]. For this reason, the concentration of donor ions is less than acceptor ones. In our system, the concentration of donor ions (Ce^{3+}) in significantly higher than acceptor concentration (Tb^{3+}). The studied system can be divided to a single Ce^{3+}-doped system and a double Ce^{3+}/Tb^{3+}-doped one. With the rise of Tb^{3+} concentration, the weight of double Ce^{3+}/Tb^{3+} system rises and the model "works" more properly. However, this reasoning requires additional checking.

The LIR approximation curves allowed obtaining absolute (S_a) and relative (S_r) temperature sensitivities according to the equations [2], [31], [32]

$$S_a = \frac{d(LIR)}{dT} \quad (3)$$

$$S_r = \frac{1}{LIR} \cdot \left|\frac{d(LIR)}{dT}\right| \cdot 100\% \quad (4)$$

The S_a and S_r curves for all the samples are represented in **Figure 6 a** and **b,** respectively.

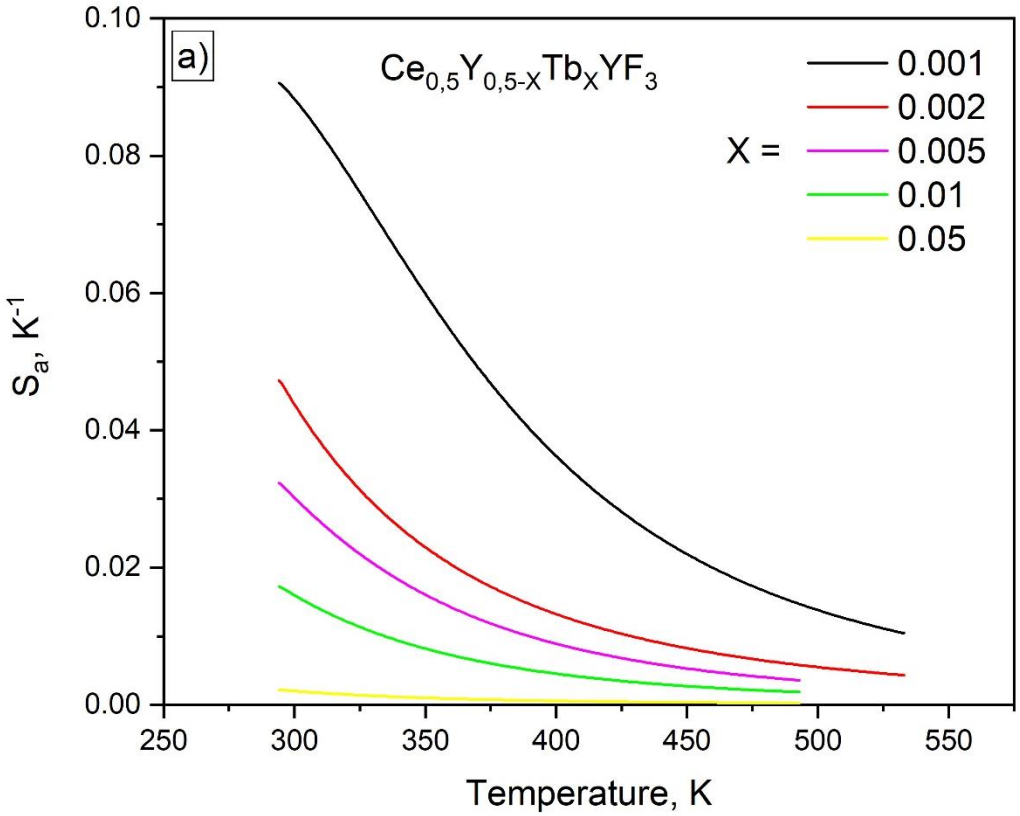

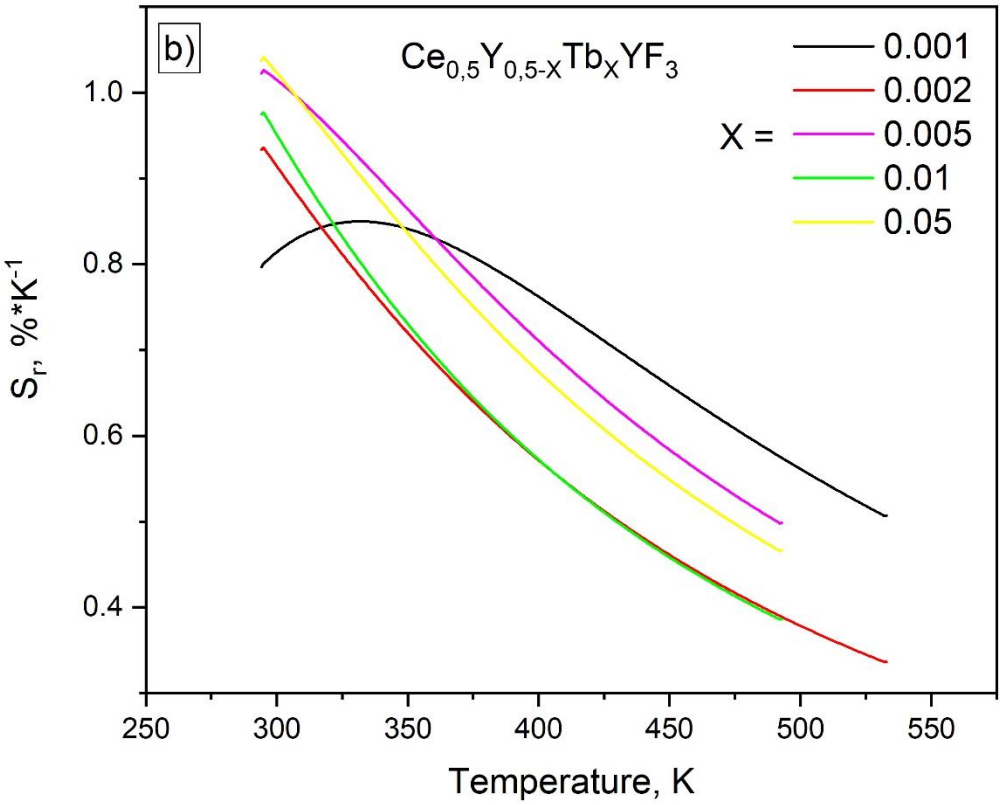

Figure 6. Absolute S_a (a) and relative S_r (b) temperature sensitivities of $Ce_{0.5}Y_{0.5-X}Tb_XF_3$ (X = 0.01, 0.02, 0.05, 0.1, and 0.5) nanoparticles

It can be seen, that $Ce_{0.5}Y_{0.5-X}Tb_XF_3$ (X = 0.01) demonstrates the highest S_a in the 303 – 353 K temperature range. Then, the S_a in this range decreases with the Tb^{3+} concentration increase. The same tendency was observed for the rate of LIR decay (Figure 5). It means that for the purpose of luminescence thermometry, the low Tb^{3+} concentrations are more preferred. The comparisons of the performances of Ce^{3+}, Tb^{3+}-based ratiometric luminescence temperature sensors are presented in Table 1.

Table 1. The comparison of luminescence thermometer performances of Ce^{3+}/Tb^{3+}-doped phosphors in the 300 – 500 K temperature range. Luminescence integrated intensity ratio (LIR) is taken as a temperature-dependent parameter

Sample	Transitions and wavelengths for LIR (I_1/I_2) and optical excitation conditions	Maximum S_a [K^{-1}] in the 300 – 500 K range	Maximum S_r [$\%K^{-1}$] in the 100 – 220 K range	Ref.
$Ce_{0.5}Y_{0.5-X}Tb_XF_3$ (X = 0.01,)	I_{Ce} (5d – 4f)/I_{Tb} ($^5D_4$ – ^7F_J, 470 – 650 K), λ_{ex} = 266 nm, pulse laser	0.19 at 303 K	1.74 (at 303 K)	This work
Ce^{3+}/Tb^{3+}: $SrAl_2Si_2O_8$	I_{Ce} (5d – 4f)/I_{Tb} ($^5D_4$ – ^7F_J,), λ_{ex} = 275 nm	~ 0.03 (at 500 K)	~ 2.0 (at 500 K)	[33]
Ce^{3+}/Tb^{3+}:LaOBr	I_{Ce} (5d – 4f)/I_{Tb} ($^5D_4$ – ^7F_J, 470 – 650 K), λ_{ex} = 254 nm.		1.4 (at 450 K)	[34]
Ce^{3+}/Tb^{3+} co-doped β-$NaYF_4$	I_{Ce} (5d – 4f)/I_{Tb} ($^5D_4$ – $^7F_5$, 542 nm), λ_{ex} = 250 nm, pulse laser	~ 0.45		[22]
Ce^{3+}/Tb^{3+}: $LiScSiO_4$	I_{Ce} (5d – 4f)/I_{Tb} ($^5D_4$ – $^7F_5$, 542 nm), λ_{ex} = 330 nm	0.005 (300 – 475 K)	~ 1.0 (at 300 K)	[35]
Ce^{3+}/Tb^{3+}:YBO_3	I_{Ce} (5d – 4f)/I_{Tb} ($^5D_4$ – $^7F_5$), λ_{ex} = 330 nm	0.07 (290 – 330 K)	0.5 (at 330 K)	[36]

Ce^{3+}/Tb^{3+}: $Na_{1.5}Y_{2.5}F_9$			~ 0.6 (at 300 K)	[37]
Ce^{3+}/Tb^{3+}:$Na_5Y_9F_{32}$	I_{Ce} (5d – 4f)/I_{Tb} ($^5D_4$ – $^7F_5$), λ_{ex} = 315 nm		1.18 (at 480 K)	[38]

It can be seen that the studied $Ce_{0.5}Y_{0.5-X}Tb_XF_3$ system demonstrates highly competitive values of both S_a and S_r. The sensitivities are larger compared to the majority of the analogs. The Ce^{3+}/Tb^{3+} co-doped β-$NaYF_4$ sample demonstrates higher S_a, however, in this system, the spectral overlap of Ce^{3+} and Tb^{3+} emissions takes place, which imposes some restrictions on the choice of LIR parameter.

The optical temperature sensors are characterized not only by the absolute and relative sensitivities but also by the minimum temperature resolution [39]. This term can be interpreted as minimum temperature difference, which can be detected via our equipment. This parameter can be calculated using the equation [39]:

$$\delta T = \frac{1}{S_r} \cdot \frac{\sigma_{LIR}}{LIR(T_{0)}} \quad (5)$$

Where σ_{LIR} is a standard deviation, T_0 is one temperature at which uncertainty is measured by repetitive measurements, S_r is the above-mentioned relative temperature sensitivity [%·K^{-1}]. The δT as a function of temperature is presented in Figure 7.

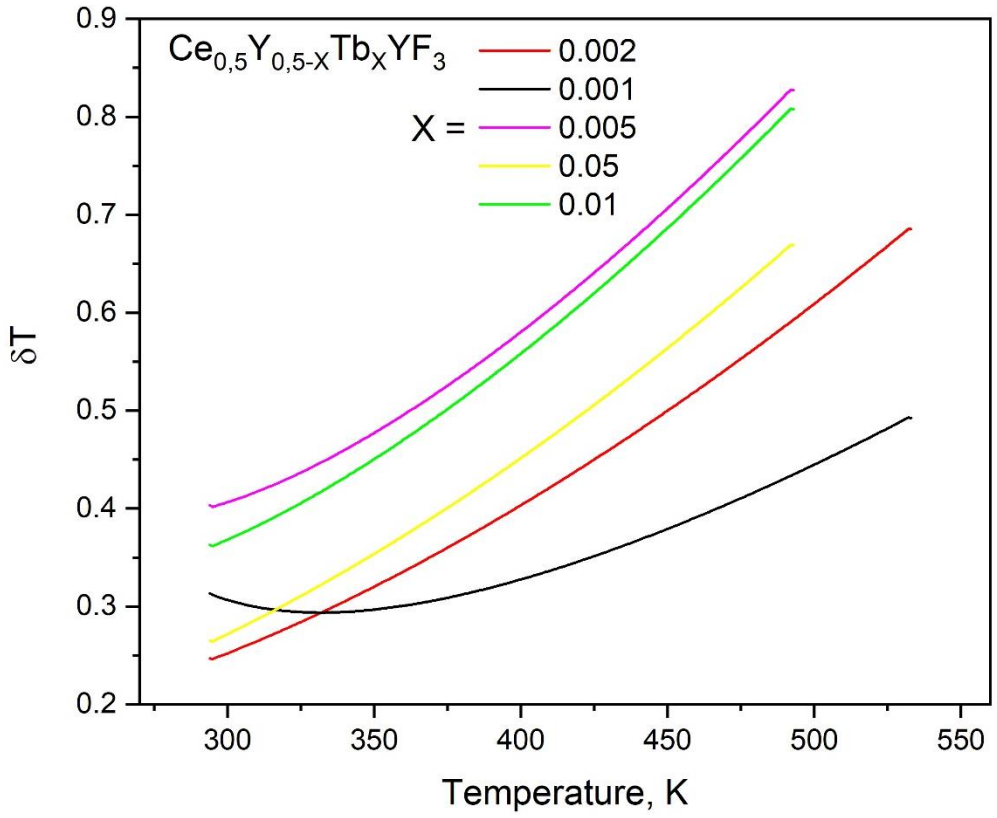

Figure 7. Temperature resolution plots of $Ce_{0.5}Y_{0.5-X}Tb_XF_3$ (X = 0.01, 0.02, 0.05, 0.1, and 0.5) nanoparticles

The values of δT are in the 0.2 – 0.8 K range. The obtained values of δT are comparable to the nowadays luminescent temperature sensors [40], [41].

Conclusions

The $Ce_{0.5}Y_{0.5-X}Tb_XF_3$ (X = 0.01, 0.02, 0.05, 0.1, and 0.5) nanoparticles were synthesized via the co-precipitation method with subsequent microwave treatment. The $Ce_{0.5}Y_{0.5-X}Tb_XF_3$ nanoparticles demonstrate a single-phase hexagonal structure corresponding to CeF_3 host. Peaks from the impurity or amorphous phases were not observed. The average diameter of the nanoparticles was 15±1 nm. The width at half maximum of the size distribution histogram was around 5 nm. To perform spectral characterization of the samples, we used pulse laser irradiation at 266 nm (4f – 5d absorption band of Ce^{3+}). All the luminescence peaks were interpreted as radiative transitions from 5d to the ground state of Ce^{3+} and $^5D_4$ – ^4F_J (J = 6, 5, 4, and 3) of Tb^{3+}. The emission peaks from $^5D_3$ level of Tb^{3+} were not observed. Probably, it t is related to the fact, that there are non-radiative transitions from $^5D_3$ to $^5D_4$. We took the luminescence integrated intensity ratio (LIR) of Ce^{3+} and Tb^{3+} luminescence peaks as a temperature-dependent parameter. The LIR functions decay with the temperature increase. Indeed, as the phonon-assisted energy transfer efficiency increases the depopulation rate of Ce^{3+} by Tb^{3+} becomes higher. In its turn, the population of $^5D_4$ of Tb^{3+} becomes more effective. Thus, the I_{Ce}/I_{Tb} decreases. However, the shape of the LIR function strongly depends on Tb^{3+} concentration. Specifically, the rate of LIR descent decreases with the increase of Tb^{3+} concentration. It was suggested that this phenomenon is related to the presence of two processes populating the $^5D_4$ state of Tb^{3+}. The first one is the phonon-assisted non-radiate transition from $^5D_3$ to $^5D_4$ of Tb^{3+} reasoning the temperature-dependence of the LIR function. The second one is cross-relaxation. In the literature, there are two proposed cross-relaxation mechanisms: $^5D_3$ – $^5D_4$ +$^7F_4$ – $^7F_0$ and $^5D_3$ – $^7F_0$ + $^7F_4$ – $^5D_4$. Both mechanisms populate $^5D_4$ state. We did

not find that these cross-relaxation processes were phonon-assisted. Suggestively, the efficiency of cross-relaxation has weak temperature dependence. Thus, there is a competition between cross-relaxations and $^5D_3$ – $^5D_4$ non-radiative transition in the population of the $^5D_4$ level. The cross-relaxation seems to be low temperature-dependent process compared to phonon-assisted non-radiative transition. Hence, the contribution of the less temperature-dependent cross-relaxation process into the population of the $^5D_4$ increases with the Tb^{3+} concentration increase compared to $^5D_3$ – $^5D_4$ non-radiative transition. This competition leads to the decrease of the LIR descent rate. It was suggested, that the concentration quenching and subsequent quenching on defects also contribute to the LIR temperature sensitivity. The maximum S_a and S_r values were 0.19 K^{-1} and 1.74 %/K at 303 K, respectively.

Funding

The synthesis of the nanoparticles, the characterization experiments via TEM and XRD were funded by the subsidy allocated to Kazan Federal University for the state assignment in the sphere of scientific activities (FZSM-2022-0021).

The temperature-dependent spectral characterization experiments were funded by the grant from the Russian Science Foundation number 22-72-00129, https://rscf.ru/project/22-72-00129/.

References

[1] Brites, C. D. S., Millán, A., & Carlos, L. D. (2016). Lanthanides in luminescent thermometry. In *Handbook on the Physics and Chemistry of Rare Earths* (Vol. 49, pp. 339-427). Elsevier., doi: 10.1016/bs.hpcre.2016.03.005.

[2] Dramićanin, M. D. (2020). Trends in luminescence thermometry. *Journal of Applied Physics*, *128*(4), doi: 10.1063/5.0014825.

[3] Brites, C. D., Lima, P. P., Silva, N. J., Millán, A., Amaral, V. S., Palacio, F., & Carlos, L. D. (2012). Thermometry at the nanoscale. *Nanoscale*, *4*(16), 4799-4829., doi: 10.1039/c2nr30663h.

[4] Piñol, R., Brites, C. D., Silva, N. J., Carlos, L. D., & Millán, A. (2019). Nanoscale thermometry for hyperthermia applications. In *Nanomaterials for Magnetic and Optical Hyperthermia Applications* (pp. 139-172). Elsevier. doi: 10.1016/B978-0-12-813928-8.00006-5.

[5] Kucsko, G., Maurer, P. C., Yao, N. Y., Kubo, M. I. C. H. A. E. L., Noh, H. J., Lo, P. K., ... & Lukin, M. D. (2013). Nanometre-scale thermometry in a living cell. *Nature*, *500*(7460), 54-58., doi: 10.1038/nature12373.

[6] Fedorov, P. P., Semashko, V. V., & Korableva, S. L. (2022). Lithium rare-earth fluorides as photonic materials: 1. Physicochemical characterization. *Inorganic Materials*, *58*(3), 223-245, doi: 10.1134/S0020168522030049.

[7] Semashko, V. V., Korableva, S. L., & Fedorov, P. P. (2022). Lithium rare-earth fluorides as photonic materials: 2. Some physical, spectroscopic, and lasing characteristics. *Inorganic Materials*, *58*(5), 447-492, doi: 10.1134/S0020168522050028.

[8] Pudovkin, M. S., Zelenikhin, P. V., Krasheninnikova, A. O., Korableva, S. L., Nizamutdinov, A. S., Alakshin, E. M., ... & Kadirov, M. K. (2016). Photoinduced toxicity of PrF 3 and LaF 3 nanoparticles. *Optics and Spectroscopy*, *121*, 538-543, doi: 10.1134/S0030400X16100209.

[9] Pudovkin, M. S., Korableva, S. L., Krasheninnicova, A. O., Nizamutdinov, A. S., Semashko, V. V., Zelenihin, P. V., ... & Nevzorova, T. A. (2014, November). Toxicity of laser irradiated photoactive fluoride PrF3 nanoparticles toward bacteria. In *Journal of Physics: Conference Series* (Vol. 560, No. 1, p. 012011). IOP Publishing, doi: 10.1088/1742-6596/560/1/012011.

[10] Zhou, S., Jiang, G., Wei, X., Duan, C., Chen, Y., & Yin, M. (2014). Pr3+-Doped β-NaYF4 for temperature sensing with fluorescence intensity ratio technique. *Journal of nanoscience and nanotechnology*, *14*(5), 3739-3742, doi: 10.1166/jnn.2014.8010.

[11] Bu, Y. Y., Cheng, S. J., Wang, X. F., & Yan, X. H. (2015). Optical thermometry based on luminescence behavior of Dy 3+-doped transparent LaF 3 glass ceramics. *Applied Physics A*, *121*, 1171-1178, doi: 10.1007/s00339-015-9483-7.

[12] Kolesnikov, I. E., Kalinichev, A. A., Kurochkin, M. A., Golyeva, E. V., Terentyeva, A. S., Kolesnikov, E. Y., & Lähderanta, E. (2019). Structural, luminescence and thermometric properties of nanocrystalline YVO4: Dy3+ temperature and concentration series. *Scientific Reports*, *9*(1), 2043.

[13] Balabhadra, S., Debasu, M. L., Brites, C. D., Nunes, L. A., Malta, O. L., Rocha, J., ... & Carlos, L. D. (2015). Boosting the sensitivity of Nd 3+-based luminescent nanothermometers. *Nanoscale*, *7*(41), 17261-17267, doi: 10.1039/c5nr05631d.

[14] Faria, W. J., Gonçalves, T. D. S., & de Camargo, A. S. (2021). Near infrared optical thermometry in fluorophosphate glasses doped with Nd3+ and Nd3+/Yb3+. *Journal of Alloys and Compounds*, *883*, 160849, doi: 10.1016/j.jallcom.2021.160849.

[15] Jin, J., Gu, Y. J., Man, C. W. Y., Cheng, J., Xu, Z., Zhang, Y., ... & Wong, W. T. (2011). Polymer-coated NaYF4: Yb3+, Er3+ upconversion nanoparticles for charge-dependent cellular imaging. *ACS nano*, *5*(10), 7838-7847, doi: 10.1021/NN201896M.

[16] Brites, C. D., Balabhadra, S., & Carlos, L. D. (2019). Lanthanide-based thermometers: at the cutting-edge of luminescence thermometry. *Advanced Optical Materials*, *7*(5), 1801239, doi: 10.1002/adom.201801239.

[17] Bednarkiewicz, A., Stefanski, M., Tomala, R., Hreniak, D., & Strek, W. (2015). Near infrared absorbing near infrared emitting highly-sensitive luminescent nanothermometer based on Nd 3+ to Yb 3+ energy transfer. *Physical Chemistry Chemical Physics*, *17*(37), 24315-24321., doi: 10.1039/c5cp03861h.

[18] Pudovkin, M. S., Ginkel, A. K., Morozov, O. A., Kiiamov, A. G., & Kuznetsov, M. D. (2022). Highly-sensitive lifetime optical thermometers based on Nd3+, Yb3+: YF3 phosphors. *Journal of Luminescence*, *249*, 119037., doi: 10.1016/j.jlumin.2022.119037.

[19] Saeed, N. A. M., Coetsee, E., & Swart, H. C. (2020). Down-conversion of YOF: Pr3+, Yb3+ phosphor. *Optical Materials*, *110*, 110516., doi: 10.1016/j.optmat.2020.110516.

[20] Ding, M., Xu, M., & Chen, D. (2017). A new non-contact self-calibrated optical thermometer based on Ce3+→ Tb3+→ Eu3+ energy transfer process. *Journal of Alloys and Compounds*, *713*, 236-247, doi: 10.1016/j.jallcom.2017.04.202.

[21] Khadiev, A. R., Korableva, S. L., Ginkel, A. K., Morozov, O. A., Nizamutdinov, A. S., Semashko, V. V., & Pudovkin, M. S. (2022). Down-conversion based Tm3+: LiY1-XYbXF4 temperature sensors. *Optical Materials*, *134*, 113118, doi: 10.1016/j.optmat.2022.113118.

[22] Ding, M., Lu, C., Chen, L., & Ji, Z. (2018). Ce3+/Tb3+ co-doped β-NaYF4 dual-emitting phosphors for self-referencing optical thermometry. *Journal of Alloys and Compounds*, *763*, 85-93, doi: 10.1016/j.jallcom.2018.05.323.

[23] Ca, N. X., Vinh, N. D., Bharti, S., Tan, P. M., Hien, N. T., Hoa, V. X., ... & Do, P. V. (2021). Optical properties of Ce3+ and Tb3+ co-doped ZnS quantum dots. *Journal of Alloys and Compounds*, *883*, 160764, doi: 10.1016/j.jallcom.2021.160764.

[24] Wang, X., Sheng, T., Fu, Z., Li, W., & Jeong, J. H. (2013). Highly uniform YF3: Ln3+ (Ln= Ce3+, Tb3+) walnut-like microcrystals: Hydrothermal synthesis and luminescent properties. *Materials Research Bulletin*, *48*(6), 2143-2148, doi: 10.1016/j.materresbull.2013.02.029.

[25] Nizamutdinov, A., Lukinova, E., Shamsutdinov, N., Zelenikhin, P., Khusainova, A., Gafurov, M., ... & Pudovkin, M. (2023). CeF3-YF3-TbF3 Nanoparticle-Polymer–"Radachlorin" Conjugates for Combined Photodynamic Therapy: Synthesis, Characterization, and Biological Activity. *Journal of Composites Science*, *7*(6), 255., doi: 10.3390/jcs7060255.

[26] Nizamutdinov, A. S., Madirov, E. I., Lukinova, E. V., Kiyamov, A. G., Andreeva, D. D., Pudovkin, M. S., ... & Semashko, V. V. (2020). Spectral-Kinetic Properties and Energy Transfer in Nanoparticles of Y 0.5–x Ce 0.5 Tb x F 3 Solid Solution. *Journal of Applied Spectroscopy*, *87*, 481-487., doi: 10.1007/s10812-020-01027-w.

[27] Bednarkiewicz, A., Stefanski, M., Tomala, R., Hreniak, D., & Strek, W. (2015). Near infrared absorbing near infrared emitting highly-sensitive luminescent nanothermometer based on Nd 3+ to Yb 3+ energy transfer. *Physical Chemistry Chemical Physics*, *17*(37), 24315-24321., doi: 10.1039/c5cp03861h.

[28] Kaczmarek, A. M., Kaczmarek, M. K., & Van Deun, R. (2019). Er 3+-to-Yb 3+ and Pr 3+-to-Yb 3+ energy transfer for highly efficient near-infrared cryogenic optical temperature sensing. *Nanoscale*, *11*(3), 833-837, doi: 10.1039/c8nr08348g.

[29] Sales, T. O., Amjad, R. J., Jacinto, C., & Dousti, M. R. (2019). Concentration dependent luminescence and cross-relaxation energy transfers in Tb3+ doped fluoroborate glasses. *Journal of Luminescence*, *205*, 282-286, doi: 10.1016/j.jlumin.2018.09.031.

[30] Solé, J., Bausa, L., & Jaque, D. (2005). *An introduction to the optical spectroscopy of inorganic solids*. John Wiley & Sons.

[31] Van Swieten, T. P., Meijerink, A., & Rabouw, F. T. (2022). Impact of noise and background on measurement uncertainties in luminescence thermometry. *ACS photonics*, *9*(4), 1366-1374, doi: 10.1021/acsphotonics.2c00039.

[32] Ćirić, A., & Dramićanin, M. D. (2022). LumTHools-Software for fitting the temperature dependence of luminescence emission intensity, lifetime, bandshift, and bandwidth and luminescence thermometry and review of the theoretical models. *Journal of Luminescence*, 119413. doi: 10.1016/j.jlumin.2022.119413.

[33] Dai, W., Hu, J., Liu, G., Xu, S., Huang, K., Zhou, J., & Xu, M. (2020). Thermometer of stable SrAl2Si2O8: Ce3+, Tb3+ based on synergistic luminescence. *Journal of Luminescence*, *217*, 116807, doi: 10.1016/j.jlumin.2019.116807.

[34] Zhang, X., Wu, Z. C., Mo, F., Li, N., Guo, Z., & Zhu, Z. (2017). Insight into temperature-dependent photoluminescence of LaOBr: Ce3+, Tb3+ phosphor as a ratiometric and colorimetric luminescent thermometer. *Dyes and Pigments*, *145*, 476-485, doi: 10.1016/j.dyepig.2017.06.032.

[35] Wu, Q., Zhou, X., Ye, S., & Ding, J. (2023). Visual ratiometric optical thermometer with high sensitivity and excellent signal discriminability based on LiScSiO4: Ce3+, Tb3+ thermochromic phosphor. *Spectrochimica Acta Part A: Molecular and Biomolecular Spectroscopy*, *294*, 122534, doi: 10.1016/j.saa.2023.122534.

[36] Li, M., You, F., Liang, C., & He, Z. (2020). Ratiometric thermal sensing based on dual emission of YBO3: Ce3+, Tb3+. *Journal of Alloys and Compounds*, *833*, 155011, doi: 10.1016/j.jallcom.2020.155011.

[37] Niu, Z., Yu, B., Xu, F., Jiang, Y., Cai, X., Hu, J., & Zhang, Y. (2022). Color-tunable luminescence and temperature sensing in Ce3+/Tb3+ co-doped transparent oxyfluoride glass-ceramics containing Na1. 5Y2. 5F9 nanocrystals. *Journal of Luminescence*, *246*, 118834, doi: 10.1016/j.jlumin.2022.118834.

[38] Xu, F., Zheng, B., Xia, H., Wang, J., Song, H., & Chen, B. (2021). Ratiometric temperature sensing behavior of dual-emitting Ce3+/Tb3+ co-doped Na5Y9F32 single crystal with high relative sensitivity. *Journal of Alloys and Compounds*, *873*, 159790, doi: 10.1016/j.jallcom.2021.159790.

[39] Ćirić, A., Stojadinović, S., & Dramićanin, M. D. (2023). Multifunctional Al2O3: Eu2+/Sm2+, 3++ Y2O3: Eu3+ Coatings Created by the Plasma Electrolytic Oxidation. *Advanced Materials Technologies*, *8*(18), 2300607, doi: 10.1002/admt.202300607.

[40] Brites, C. D., Fiaczyk, K., Ramalho, J. F., Sójka, M., Carlos, L. D., & Zych, E. (2018). Widening the temperature range of luminescent thermometers through the intra-and interconfigurational transitions of Pr3+. *Advanced Optical Materials*, *6*(10), 1701318, doi: 10.1002/adom.201701318.

[41] Ananias, D., Firmino, A. D., Mendes, R. F., Paz, F. A. A., Nolasco, M., Carlos, L. D., & Rocha, J. (2017). Excimer formation in a terbium metal–organic framework assists luminescence thermometry. *Chemistry of Materials*, *29*(21), 9547-9554, doi: 10.1021/acs.chemmater.7b03817.